

Chemical Science

Accepted Manuscript

This article can be cited before page numbers have been issued, to do this please use: Z. Qin, H. Zhuang, D. Song, G. Zhang, H. Gao, X. Du, M. Jiang, P. Zhang and J. Gong, *Chem. Sci.*, 2025, DOI: 10.1039/D4SC08219B.



This is an Accepted Manuscript, which has been through the Royal Society of Chemistry peer review process and has been accepted for publication.

Accepted Manuscripts are published online shortly after acceptance, before technical editing, formatting and proof reading. Using this free service, authors can make their results available to the community, in citable form, before we publish the edited article. We will replace this Accepted Manuscript with the edited and formatted Advance Article as soon as it is available.

You can find more information about Accepted Manuscripts in the [Information for Authors](#).

Please note that technical editing may introduce minor changes to the text and/or graphics, which may alter content. The journal's standard [Terms & Conditions](#) and the [Ethical guidelines](#) still apply. In no event shall the Royal Society of Chemistry be held responsible for any errors or omissions in this Accepted Manuscript or any consequences arising from the use of any information it contains.

ARTICLE

Tuning the microenvironment of immobilized molecular catalyst for selective electrochemical CO₂ reduction

Ziying Qin,^a Haocheng Zhuang,^a Dayou Song,^a Gong Zhang,^a Hui Gao,^a Xiaowei Du,^a Mingyang Jiang,^a Peng Zhang,^{*abcdef} and Jinlong Gong^{*abcdefg}

Received 00th January 20xx,
Accepted 00th January 20xx

DOI: 10.1039/x0xx00000x

Electrochemical CO₂ reduction reaction (CO₂RR), as a novel technology, holds great promise for carbon neutrality. Immobilized molecular catalysts are considered efficient CO₂RR catalysts due to their high selectivity and fast electron transfer rates. However, at high current densities, changes in the microenvironment of molecular catalysts result in a decrease in local CO₂ concentration, leading to suboptimal catalytic performance. This work describes an effective strategy to control the local CO₂ concentration by manipulating the hydrophobicity. The obtained catalyst exhibits high CO selectivity with Faradaic efficiency (FE) of 96% in a membrane electrode assembly. Moreover, a consistent FE exceeding 85% could be achieved with a total current of 0.8 A. Diffusion impedance testing and interface characterization confirm that the enhanced hydrophobicity of the catalyst layer leads to an increase in the thickness of the Nernst diffusion layer and an expansion of the three-phase interface, thereby accelerating CO₂ adsorption to enhance the performance.

Introduction

Due to the massive consumption of fossil fuels, CO₂ emissions are accumulating in the atmosphere progressively.^{1–3} Electrochemical CO₂ reduction reaction (CO₂RR) is a promising technology for achieving carbon neutrality and closing the carbon loop.^{4–8} In CO₂RR, molecular catalysts exhibit outstanding tunability, the microenvironment and electronic states of which could be controlled through the design of the molecular structure.^{9,10} As a result, there has been a growing interest in the rational design and optimization of molecular catalysts for CO₂RR in recent years.^{11–13}

Molecular catalysts can be utilized in homogeneous and heterogeneous approaches.¹⁴ In homogeneous catalysis, molecular catalysts must undergo diffusion to facilitate electron transfer.^{15,16} In comparison, heterogenization immobilizes molecular catalysts onto supports, allowing electrochemical reactions to occur with adsorbed molecular species on the electrode.¹⁷ The heterogenization strategy of molecular catalysts offers the advantages of fast electron transport,¹⁸ high catalyst spatial density,¹⁹ and compatibility with commercial

electrolyzers.²⁰ As a result, extensive efforts have been dedicated to the quest for high-performance molecular catalysts and immobilization methods. To date, cobalt-containing molecular catalysts with macrocyclic ligands, particularly cobalt phthalocyanine (CoPc), have emerged as the most selective and active candidates for CO₂RR.²¹ Immobilizing CoPc on conductive supports to enable heterogeneous catalysis has been a significant focus,^{22–24} applicable in the fields of electrocatalytic oxygen reduction/evolution reactions,^{25,26} CO electroreduction to methanol,²⁷ and CO₂ electroreduction to CO.²⁸ For electrochemical CO₂ reduction to CO, immobilized CoPc exhibits relatively good performance. Its molecular mechanism primarily centers on the coordination chemistry of the metal-N₄ active site and dynamic reaction pathways.^{29,30} The metal center of CoPc strongly adsorbs CO₂ to form *CO₂, which then undergoes multiple electron-proton transfers to produce CO. However, its electrochemical performance is only sustained within a low current density range.³¹ Typically, methods such as adding ligands to improve Co site dispersion or modulating the electronic structure of the Co center are employed to maintain Faradaic efficiency (FE) at high current densities (current density > 100 mA/cm², FE > 80%).²⁸ The reasons for this result are twofold: at high current densities, CoPc tends to aggregate, leading to active site coverage; additionally, the microenvironment of CoPc is disrupted—specifically, proton transport accelerates, and local CO₂ concentration decreases.³² These factors together result in a decline in the performance of immobilized CoPc. While there have been many reports addressing CoPc aggregation at high current densities, there is still a lack of research on improving the microenvironment of CoPc. Mechanistically, the CO₂RR performance of immobilized CoPc is critically influenced by the local CO₂ concentration.³³ This is because the adsorption and activation of CO₂ serve as the rate-determining step (RDS) in CO₂RR towards CO.^{34–36} At the same time, the competitive proton reduction reaction to generate H₂ would affect the selectivity. Consequently,

^a School of Chemical Engineering & Technology, Key Laboratory for Green Chemical Technology of Ministry of Education, Tianjin University; Collaborative Innovation Center for Chemical Science & Engineering; Tianjin, 300072, China.

^b Joint School of National University of Singapore and Tianjin University, International Campus of Tianjin University, Binhai New City, Fuzhou 350207, China

^c International Joint Laboratory of Low-carbon Chemical Engineering of Ministry of Education, Tianjin 300350, China

^d Haihe Laboratory of Sustainable Chemical Transformations, Tianjin 300192, China

^e National Industry-Education Platform of Energy Storage, Tianjin University, 135 Yaguan Road, Tianjin, 300350, China

^f Tianjin Normal University, Tianjin, 300387, China

^g State Key Laboratory of Synthetic Biology, Tianjin University, Tianjin, 300072, China

† Supplementary Information available: [details of any supplementary information available should be included here]. See DOI: 10.1039/x0xx00000x



the control of local CO₂ concentration not only facilitates the manipulation of product selectivity but also regulates the reaction rate, as illustrated in Figure 1.

View Article Online
DOI: 10.1039/D4SC08219B

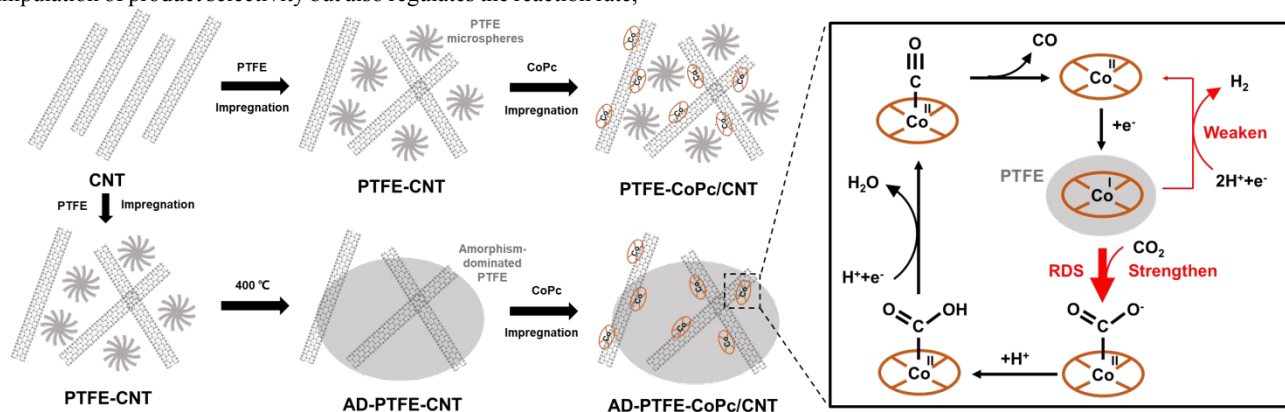


Figure 1. Synthesis and catalytic mechanism of PTFE-CoPc/CNT and AD-PTFE-CoPc/CNT.

Polytetrafluoroethylene (PTFE) modification is a commonly used approach to enhance the hydrophobicity of catalyst layers, and it has been widely applied to suppress the hydrogen evolution reaction of metal catalysts (such as Ag,³⁷ Cu,³³ Bi,³⁸ Ni,³⁹ etc.). However, there is still a lack of research on controlling the hydrophobicity of molecular catalysts. Additionally, the modification process of PTFE lacks precise control, making it difficult to achieve uniform dispersion of PTFE and strengthen the interaction between the catalyst and PTFE. Therefore, rationally designing the modification strategies of PTFE for molecular catalysts, manipulating the microenvironment of molecular catalysts to enhance local CO₂ concentration, and improving catalytic performance through control of RDSs continue to be critical issues in need of further investigation.

In this work, we report a strategy for controlling the local CO₂ concentration of the immobilized molecular catalysts by manipulating the hydrophobicity of the catalyst layer. Through melt crystallization, the volume restriction of CNTs hinders the incorporation of large polymer chains into the lattice, resulting in the reduction of PTFE crystallinity. Consequently, CoPc/CNT modified with amorphism-dominated PTFE was obtained (AD-PTFE-CoPc/CNT). The loose arrangement of polymer chains in AD-PTFE-CoPc/CNT causes free volume expansion, providing richer microscale hydrophobic environment, which facilitates CO₂ transfer at the interface, and ultimately enhances the catalytic performance of the molecular catalyst. Specifically, a carbon monoxide Faradaic efficiency (FE_{CO}) of 96% at a current density of 75 mA/cm² was achieved. Furthermore, at a higher current density of 200 mA/cm², FE_{CO} can still be maintained at over 85%. This study presents a strategy for controlling the microenvironment of CoPc catalysts and holds promise for transferring these results to other molecular catalysts, which is of significant importance for the industrial application of molecular catalysts.

Results and discussion

Preparation and structure characterization

We presented a synthetic route to prepare immobilized molecular catalysts with varied hydrophobicity by controlling the crystallinity of

PTFE, as shown in Figure 1. Using the equal-volume impregnation method, PTFE powder was dispersed in *t*-BuOH as the impregnating agent, resulting in a stable PTFE dispersion that remained intact for 3 hours (Figure S1). Under ultrasonic action, the PTFE dispersion was uniformly mixed with CNT powder, leading to the preparation of PTFE-modified carbon nanotubes (PTFE-CNT). Subsequently, CoPc was well dispersed in DMF and immobilized onto CNT, forming PTFE-CoPc/CNT due to the π - π conjugation effect.⁴⁰ The treatment temperature was identified as a crucial factor influencing the crystallinity of the PTFE.⁴¹ A 2-hour incubation at a high temperature was employed to facilitate the diffusion of molten PTFE, followed by cooling to induce crystallization. The interface adhesion between PTFE and CNT hindered the movement of long PTFE polymer chains, impeding their incorporation into the lattice. This effect resulted in the preferential growth of PTFE in an amorphous state within the three-dimensional framework of CNT. The polymer chains in the amorphous regions were arranged in a more disordered and loose manner, leading to a decrease in crystallinity, reduced PTFE density, and volume expansion, thereby providing a larger hydrophobic surface area for the CNT. Additionally, the appearance of heterogeneous nucleation at phase interfaces facilitated a tighter binding between PTFE and CNT. Consequently, high-temperature treatment resulted in the formation of AD-PTFE-CNT material with enhanced hydrophobic properties. Subsequently, CoPc was immobilized on AD-PTFE-CNT using the same method as PTFE-CNT, yielding AD-PTFE-CoPc/CNT. This method allows for controlling the hydrophobicity of the molecular catalysts by regulating the processing temperature.

Scanning electron microscope (SEM) was employed to investigate the morphological impact of high-temperature treatment on PTFE. For PTFE-CoPc/CNT, PTFE appeared nearly spherical and was dispersed around the carbon nanotubes (Figure 2a, b). This result indicates that PTFE dispersed in *t*-BuOH tends to produce a physically dispersed suspension, remaining undissolved and thereby preserving the original crystalline state of PTFE. For AD-PTFE-CoPc/CNT, PTFE was transitioned from spherical state to amorphous state (Figure 2c). This transformation can be attributed to the presence of a second phase during PTFE crystallization, which hinders the movement of PTFE molecules and negatively impacts the crystal growth.^{42,43} As



shown in Figure 2d, there was an interface bonding between PTFE and CNT, with PTFE filling the three-dimensional network voids of CNT. During crystallization, bonding hampered the mobility of PTFE polymer chains, making it difficult for them to fold and arrange in an orderly manner to form spherical crystals. Furthermore, the presence of a second phase, CNT, led to an increase in the number of crystal nuclei and thus enhanced interactions between crystals,⁴⁴ increasing the entanglement of PTFE and consequently expanding the amorphous region. The dispersion of PTFE was observed using

electron dispersive X-ray spectroscopy (EDS) mappings (Figure S2 and S3). The characteristic fluorine (F) element of PTFE exhibited aggregation states in PTFE-CoPc/CNT, whereas the F element was well-dispersed in AD-PTFE-CoPc/CNT. Aberration-corrected transmission electron microscopy (AC-TEM) was used to identify the CoPc sites loaded on AD-PTFE-CNT (Figure 2e). Co appeared to be approximate single atoms, and no obvious aggregation occurred. Highly dispersed CoPc showed isolated high Z-contrast spots in AC-TEM images, highlighted by red dashed circles.

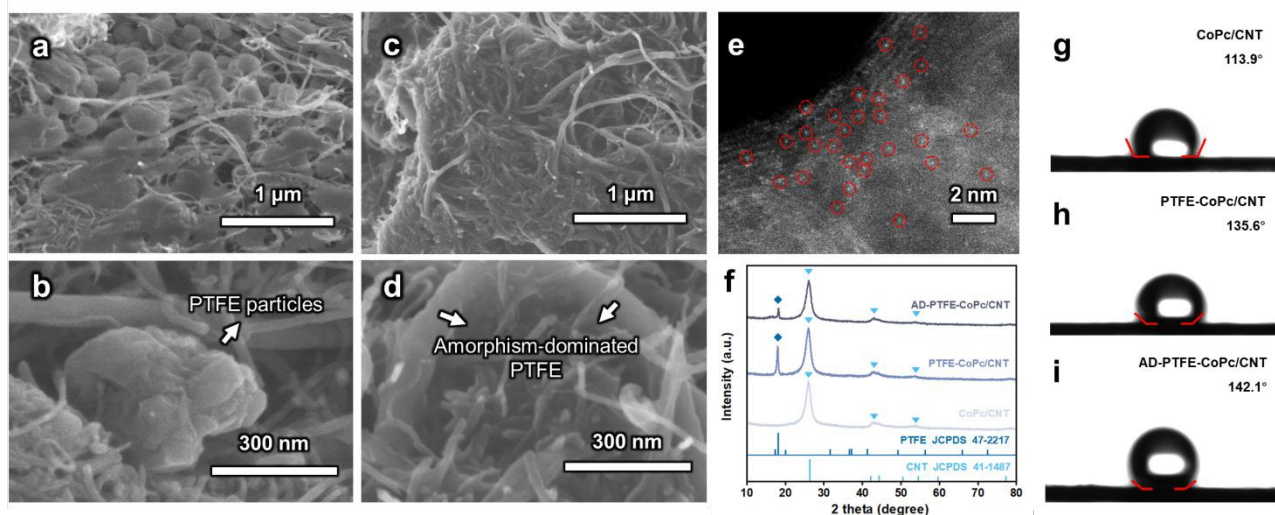


Figure 2. SEM images of the electrode loaded with (a, b) PTFE-CoPc/CNT, (c, d) AD-PTFE-CoPc/CNT. (e) AC-TEM image of AD-PTFE-CoPc/CNT. (f) XRD patterns of CoPc/CNT, PTFE-CoPc/CNT and AD-PTFE-CoPc/CNT. (g-i) Contact angles of CoPc/CNT, PTFE-CoPc/CNT and AD-PTFE-CoPc/CNT with a drop of water.

To investigate the crystallinity of PTFE, X-ray diffraction (XRD) patterns of CoPc/CNT, PTFE-CoPc/CNT, and AD-PTFE-CoPc/CNT were obtained (Figure 2f). The peak at 18.0° corresponded to the characteristic peak of the PTFE crystal,⁴⁵ while peaks at 26.0° and 42.8° was assigned to the CNT.⁴⁶ Compared with PTFE-CoPc/CNT, the PTFE diffraction peak of AD-PTFE-CoPc/CNT was significantly reduced, indicating that PTFE transformed from crystalline to amorphous form, consistent with the SEM observation results. No diffraction signal of CoPc was observed in the XRD results, which may be caused by the low and well-dispersed CoPc content in the catalyst.

The mass content of CoPc can be obtained by inductively coupled plasma mass spectrometry (ICP-MS). The mass fractions of Co, the characteristic element of CoPc, for CoPc/CNT, PTFE-CoPc/CNT, and AD-PTFE-CoPc/CNT were 0.14%, 0.08%, and 0.07%, respectively

(Table S1). This result is likely attributable to the increased hydrophobicity resulting from the incorporation of PTFE, which impacted the loading of CoPc on CNTs. The element states and surface compositions of catalysts were characterized by X-ray photoelectron spectroscopy (XPS). Compared to CNT, CoPc/CNT, PTFE-CoPc/CNT, and AD-PTFE-CoPc/CNT showed the same peak positions at binding energies of 780.6 and 795.9 eV (Figure S4a), which corresponded to the characteristic peaks of Co 2p_{3/2} and 2p_{1/2}. These observations indicate the successful loading of CoPc onto the material surface, with no apparent peak shifts observed, suggesting that the introduction of PTFE does not affect the binding of CoPc with CNT. As shown in Figure S4b, the spectral signal of F element at

689.9 eV was detected in PTFE-CoPc/CNT and AD-PTFE-CoPc/CNT, the high-temperature treatment process did not change the F element state, and it is speculated that PTFE only undergoes the change of crystallinity to construct a hydrophobic environment, thereby altering material properties.

To investigate the impact of PTFE crystallinity changes on the hydrophobicity of the catalyst layer, contact angles of water were measured on gas diffusion electrode (GDEs) coated with catalysts. The contact angle of bare carbon paper was measured at 146.8° (Figure S5a), which decreased to 113.9° after loading with CoPc/CNT (Figure 2g), indicating the hydrophilic nature of the CoPc/CNT. Pure PTFE exhibited superhydrophobicity with a contact angle of 153.1° (Figure S5b). The contact angle of water on PTFE-CoPc/CNT (135.6°) was lower than for AD-PTFE-CoPc/CNT (142.1°) (Figure 2h and i), suggesting that high-temperature treatment significantly improved the hydrophobicity of the electrode. This was because high-temperature treatment caused the three-dimensional structure of the spherulites to unfold, resulting in an increased surface area due to deviations from the spherical crystalline structure and free volume expansion.⁴⁷

Performance of CO₂RR

PTFE modifies the hydrophobicity of the catalyst layer, inevitably affecting the performance of the GDE. The CO₂RR electrocatalytic activity of GDE was evaluated in a typical three-electrode flow cell reactor. As shown in Figure 3a, at -1.5 V versus the reversible hydrogen electrode (RHE, all potentials were reported with respect to this reference in this paper), CoPc/CNT exhibited a current density of



160.2 mA/cm², higher than that of PTFE-CoPc/CNT (83.9 mA/cm²) and AD-PTFE-CoPc/CNT (113.6 mA/cm²). The introduction of PTFE has influenced the electrochemical response of the catalyst, attributed to the lower electrical conductivity of PTFE,⁴⁸ affecting the formation of a three-dimensional conductive network of CNTs in the PTFE-CNT hybrid system,⁴⁹ which impedes the charge transfer process in the catalyst layer, resulting in a decrease in the rate of electrocatalytic reactions. AD-PTFE-CoPc/CNT exhibited an enhanced current density compared to PTFE-CoPc/CNT, attributed to the higher hydrophobicity of AD-PTFE-CoPc/CNT, which increased the local CO₂ concentration, consequently enhancing the rate of catalytic reactions and the current density. The turnover frequency (TOF) was a critical and commonly used metric for assessing the

intrinsic activity of molecular catalysts. Figure S6 presents the potential-dependent TOF for CoPc/CNT, PTFE-CoPc/CNT, and AD-PTFE-CoPc/CNT. TOF steadily increased with an increase in working potential, reaching 20.6 s⁻¹ for PTFE-CoPc/CNT and 36.7 s⁻¹ for AD-PTFE-CoPc/CNT at -1.0 V, maintaining an upward trend even at high currents. The TOF of CoPc/CNT was the lowest within the tested potential range (-0.6 V to -1.0 V). This result indicated that the enhanced hydrophobic environment improved the performance of active sites. Despite a lower number of active sites (Table S1), superior catalytic performance was achieved due to the favorable local environment. Therefore, in catalyst design, it is crucial to balance the effects of increased hydrophobicity on active site loading and local CO₂ concentration in order to optimize catalytic performance.

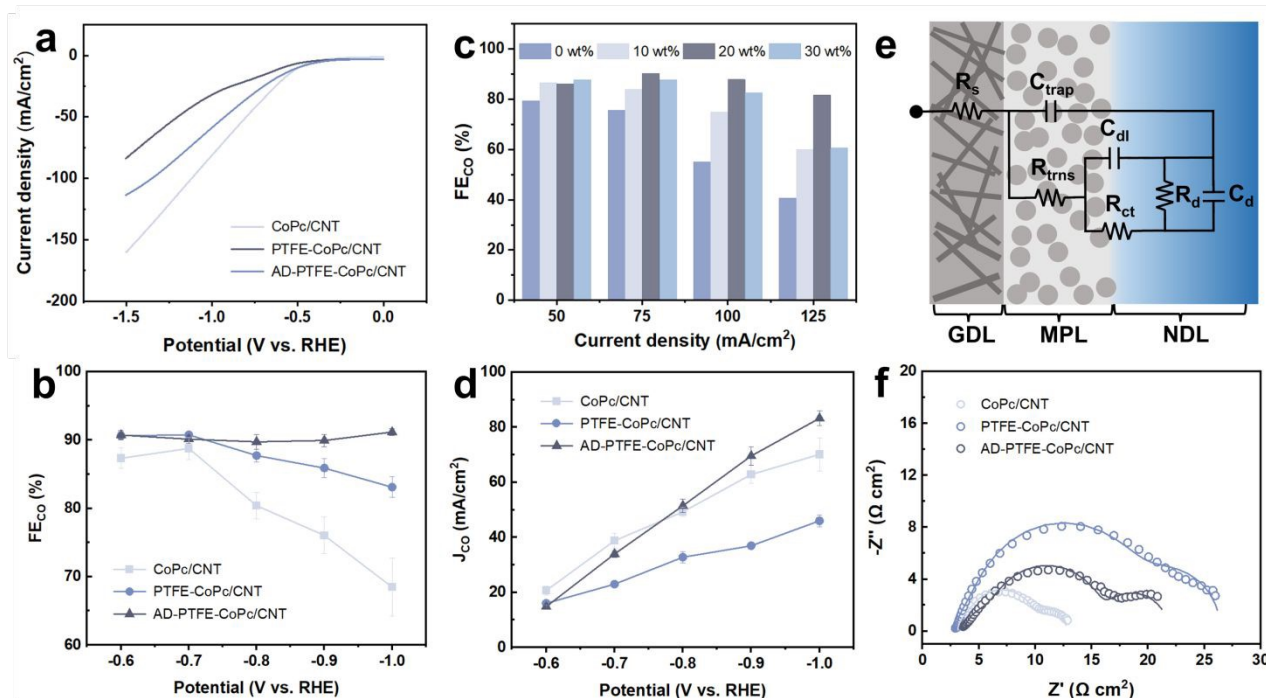


Figure 3. (a) LSV curves, (b) FE_{CO} of CoPc/CNT, PTFE-CoPc/CNT, and AD-PTFE-CoPc/CNT. (c) FE_{CO} of AD-PTFE-CoPc/CNT with 0 wt%, 10 wt%, 20 wt% and 30 wt% PTFE. (d) J_{CO} of CoPc/CNT, PTFE-CoPc/CNT, and AD-PTFE-CoPc/CNT. (e) Circuit model for porous carbon electrodes. (f) EIS spectra acquired for the CoPc/CNT, PTFE-CoPc/CNT, and AD-PTFE-CoPc/CNT electrodes under CO₂RR conditions (-0.4 V) in a flow cell reactor. Symbols are experimental data, and lines are fittings with the circuit model in (e).

To assess the impact of hydrophobic treatment on the selectivity of CO₂ conversion, the detection of CO₂ conversion products was performed at specific potentials. H₂ and CO were identified as the main products (Figure S7-S9). Within the potential range of -0.6 V to -1.0 V, both PTFE-CoPc/CNT and AD-PTFE-CoPc/CNT exhibited FE_{CO} exceeding 85% (Figure 3b), significantly higher than CoPc/CNT (Figure S7), and this difference widened with increasing potential. This result could be attributed to the accelerated water transfer as the current increased, the enhanced electrode hydrophobicity impeding water transport, thus maintaining a certain local CO₂ concentration. Furthermore, AD-PTFE-CoPc/CNT achieved the highest selectivity and maintained stability within the test potential range (Figure S9), owing to its superior hydrophobicity. Since direct physical mixing of PTFE into the ink was a common strategy,³³ comparing the performance of PTFE-ink-CoPc/CNT obtained by this method was particularly important. The performance of PTFE-ink-CoPc/CNT was essentially similar to that of PTFE-

CoPc/CNT, likely because the PTFE in both cases was in particulate form, resulting in similar effects (Figure S10). The Nuclear magnetic resonance (NMR) spectra of the electrolyte collected from the flow cell reactor revealed no signal peaks other than water (Figure S11 and S12), indicating that barely any liquid products were generated during CO₂RR. Additionally, the effect of PTFE content on overall performance was investigated for AD-PTFE-CoPc/CNT, with PTFE contents of 0 wt%, 10 wt%, 20 wt%, and 30 wt% tested under constant current conditions in the current range of 50-125 mA/cm². FE_{CO} exhibited the volcanic trend with increasing PTFE content at all current densities, reaching a maximum FE_{CO} of 92% when the PTFE content was 20 wt% under a current density of 75 mA/cm² (Figure 3c). At 100 mA/cm², the FE_{CO} exhibited a volcanic trend with increasing amorphism-dominated PTFE content. FE_{CO} significantly increased from 55% without PTFE to 88% with 20 wt% PTFE (Figure S13). This result suggested that enhancing the loading at low contents improved hydrophobicity and thereby enhanced electrode



performance. However, at high contents, it might affect catalyst loading and electron transfer on the electrode surface.

To comprehensively investigate the impact of increased hydrophobicity on electrode activity and selectivity, the partial current density of CO (J_{CO}) was obtained (Figure 3d). Due to its lower conductivity, PTFE-CoPc/CNT exhibited relatively lower J_{CO} . At -0.8 V, J_{CO} for AD-PTFE-CoPc/CNT started to surpass that of CoPc/CNT,

reaching 84.0 mA/cm² at -1.0 V. AD-PTFE-CoPc/CNT demonstrated superior overall performance at high currents compared to CoPc/CNT. Half-cell cathodic energy efficiency (CEE) was a crucial parameter for assessing the energy consumption. PTFE significantly reduced energy consumption, with this effect being particularly pronounced at high potentials (Figure S14).

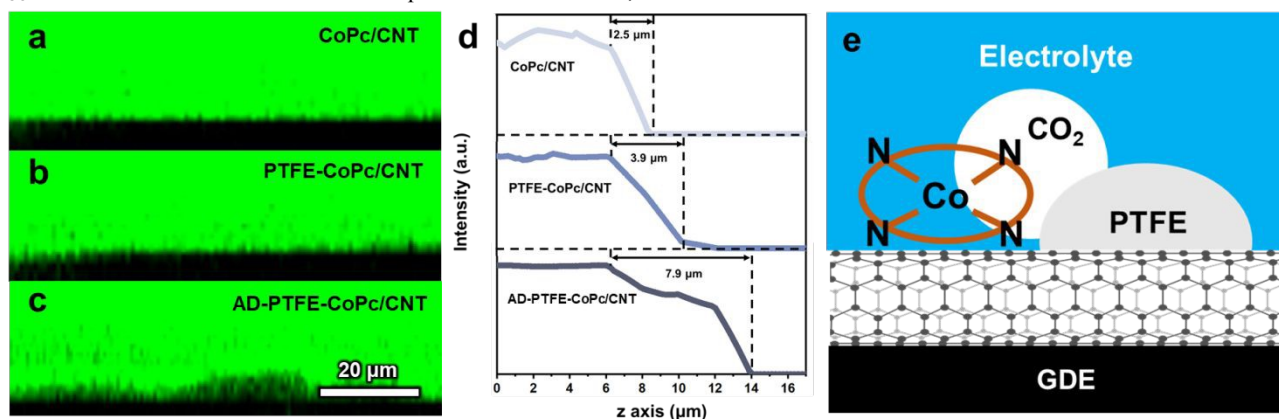


Figure 4. (a-c) Cross-section fluorescence images of electrodes coated with CoPc/CNT, PTFE-CoPc/CNT and AD-PTFE-CoPc/CNT. (d) Corresponding z axis fluorescence intensity line scans of (a-c). (e) Schematic illustration of the impact of PTFE on the local CO₂ and CoPc microenvironment.

To quantitatively elucidate the impact of hydrophobicity in the catalyst layer on CO₂RR, electrochemical impedance spectroscopy (EIS) was employed to investigate the diffusion of CO₂ in CO₂RR. In GDE system, the Nernst diffusion layer (NDL) is defined as the virtual layer with a CO₂ concentration gradient from the electrode surface to the bulk concentration.³⁸ A thinner NDL indicates a higher local CO₂ concentration. Therefore, by examining the thickness of the NDL (δ), the CO₂ transport in the microporous layer (MPL) can be assessed. A ladder circuit was used to model the impedance of GDE (Figure 3e).⁵⁰ Here, R_{ct} represents the charge transfer resistance in the electrochemical reaction. R_d and C_d are the resistance and capacitance of the NDL, respectively, and D is the diffusion coefficient of CO₂. The thickness of the NDL can be calculated using the formula $\delta = \sqrt{3R_d C_d D}$.⁵¹ EIS spectra for the CO₂RR conditions in a flow cell were obtained and fitted with the circuit model shown in Figure 3e. Figure 3f revealed a prominent diffusion impedance in the low-frequency region, indicating that the electrode was highly sensitive to local CO₂ concentration, and CO₂ diffusion was a key factor influencing CO₂RR performance, especially for molecular catalysts. The fitting results, as shown in Table S2, revealed that the diffusion layer thickness for CoPc/CNT, PTFE-CoPc/CNT, and AD-PTFE-CoPc/CNT were 3.76 μm, 3.12 μm, and 1.05 μm, respectively. A reduced diffusion layer thickness improved CO₂ mass transfer, resulting in a higher local CO₂ concentration at the catalyst surface, which promoted CO₂ coordination adsorption and enhanced reaction selectivity, manifested as a higher FE_{CO} . In addition, since the electrochemical surface area (ECSA) is proportional to the double-layer capacitance (C_{dl}), the C_{dl} obtained from EIS can reflect ECSA.⁵² ECSA refers to the portion of an electrode's surface that is in contact with and accessible to the electrolyte.^{38,53} The C_{dl} decreased from 1.88 mF in the CoPc/CNT electrode to 1.20 mF in the PTFE-CoPc/CNT electrode, and further dropped to 0.86 mF in the AD-PTFE-CoPc/CNT (Table S2). This demonstrated that PTFE particles can enhance the hydrophobicity of

the electrode, with amorphism-dominated PTFE further amplifying this effect. Thus, variations in ECSA indicated differing degrees of three-phase interface contact, which in turn influenced catalytic activity. Although AD-PTFE-CoPc/CNT has a relatively small ECSA compared with the other samples, it still exhibited the best performance, confirming the effectiveness of tuning the microenvironment. Furthermore, CoPc/CNT had the lowest R_{ct} (4.25 Ω·cm²) due to PTFE introduction restricting electron transfer, while AD-PTFE-CoPc/CNT exhibited lower R_{ct} (6.96 Ω·cm²) compared to PTFE-CoPc/CNT (12.1 Ω·cm²) due to the larger local CO₂ concentration reducing electrochemical reaction resistance. This effect facilitated CO₂RR and the corresponding electron transfer, resulting in higher catalytic activity, higher current density, and TOF.

Characterization of hydrophobic interfaces

Confocal laser scanning microscopy (CLSM) was employed to observe the microenvironment at the interface, further corroborating the relationship between electrode hydrophobicity and local CO₂ concentration.⁵⁴ To determine the microscale contact state of the three electrodes, cross-section images along the z-axis were compared. Figure 4a-c displayed the cross-section structures of CoPc/CNT, PTFE-CoPc/CNT, and AD-PTFE-CoPc/CNT, respectively. As shown in Figure 4b and c, there were numerous non-luminescent spots at the contact interface of PTFE-CoPc/CNT and AD-PTFE-CoPc/CNT, which were occupied by the gas phase and increase the degree of liquid-gas interface contact. This was further confirmed by analyzing the fluorescence intensity decay along the z-axis (Figure 4d). Due to the strong light absorption and blocking effect of the solid phase, the typical decay distance at the liquid-solid interface is significantly shorter than that at the liquid-gas interface. The decay distance of CoPc/CNT was 2.5 μm, which was typical of a liquid-solid interface. For PTFE-CoPc/CNT and AD-PTFE-CoPc/CNT, the decay distances



increased to 3.9 and 7.9 μm , respectively, indicating that the liquid-gas interface gradually replaced the liquid-solid interface. AD-PTFE-CoPc/CNT exhibited the highest level of hydrophobicity, consequently displaying the most significant liquid-gas interface. Additionally, cross-section SEM revealed that the catalyst layer thickness for all three electrodes was approximately the same (Figure S15). Hence, the variation in catalyst layer hydrophobicity and local CO_2 concentration was not induced by changes in thickness. Thus, it could be concluded that the presence of PTFE facilitated CO_2 mass transport, maintaining a high CO_2 concentration near the CoPc sites, thereby enhancing both the selectivity and activity of CO_2RR (Figure 4e).

Industrial current performance in a membrane electrode assembly (MEA)

Membrane electrode assembly (MEA) with an effective area of 4 cm^2 was employed to test the industrial operation of catalysts. AD-PTFE-CoPc/CNT exhibited a consistent selectivity of over 90% within the current range of 0–100 mA/cm^2 (Figure 5a and Figure S16). In contrast, PTFE-CoPc/CNT and CoPc/CNT exhibited a decreased FE_{CO} to 75% and 57%, respectively, at 100 mA/cm^2 (Figure S17 and S18). AD-PTFE-CoPc/CNT maintained a FE_{CO} of over 85% at current density expanded to 200 mA/cm^2 (Figure 5b), which was possibly due to the absence of the cathodic electrolyte in MEA system, leading to an increased local CO_2 concentration. As shown in Figure S19, AD-PTFE-CoPc/CNT exhibited stable operation for 3 hours without electrode flushing, maintaining a FE_{CO} of over 85%. The gradual increase in operating voltage was likely due to the salt precipitation during the reaction, which increases the overall resistance of the reactor. The stability of the catalyst layer improved with the addition of either PTFE or amorphism-dominated PTFE. This indicates that, under high current conditions, creating a microscale hydrophobic environment not only maintained a high FE_{CO} but also enhanced the electrode's long-term stability. To investigate the chemical and structural stability of the electrocatalysts, the electrode loaded with AD-PTFE-CoPc/CNT was characterized in the pristine state and after the reaction. The results of EDS and SEM indicated that the morphology of AD-PTFE-CNT remained unchanged (Figure S20, S21a and b). XRD results further confirmed the crystallinity of PTFE is stable (Figure S21c). XPS was further employed to monitor the change of the chemical state of CoPc (Figure S21d). The positions of the characteristic peaks of Co 2p remain consistent after the reaction compared to those of the pristine CoPc sample, suggesting that the chemical state of Co is stable during the electrochemical reaction. AC-TEM image of AD-PTFE-CoPc/CNT after the reaction showed that Co sites still appeared to be approximate single atoms with good dispersion, indicating the structural stability of the sample (Figure S22). To investigate the effect of the reaction on the hydrophobic environment of the catalyst layer, CLSM characterization of the GDE coated with AD-PTFE-CoPc/CNT after the reaction was conducted. The result showed that the fluorescence decay distance along the z-axis after the reaction was 7.0 μm , which was almost unchanged compared to 7.9 μm in the pristine state (Figure S23 and S24). Additionally, the contact angle of the electrode after the reaction was measured, which was 145°, nearly unchanged from 142.1° in the pristine state (Figure S25). Therefore, the reaction had little impact on

the hydrophobic environment of the catalyst layer. Additionally, AD-PTFE-CoPc/CNT exhibited superior J_{CO} (96.40 mA/cm^2 at 100 mA/cm^2), demonstrating noteworthy electrochemical activity (Figure 5c), which could also be explained by TOF (41.3 s^{-1} at 100 mA/cm^2 , Figure S26). PTFE-CoPc/CNT and AD-PTFE-CoPc/CNT showed a narrower decrease in energy efficiency (EE) than CoPc/CNT with increasing current (Figure 5d). AD-PTFE-CoPc/CNT still maintained an EE of over 40% at 100 mA/cm^2 , likely due to its lower reaction resistance and thicker diffusion layer, thus reducing reaction impedance and overpotential.

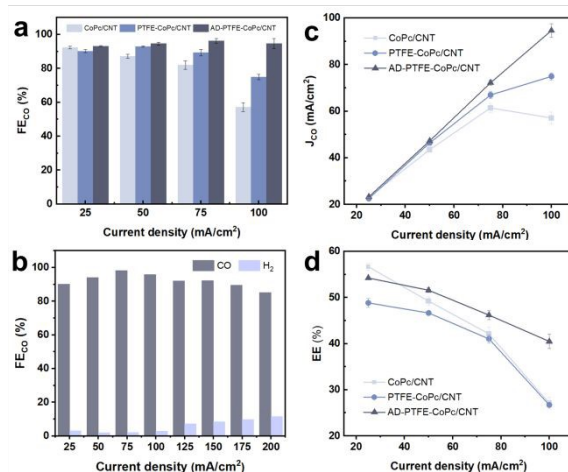


Figure 5. (a) FE_{CO} for CoPc/CNT, PTFE-CoPc/CNT, and AD-PTFE-CoPc/CNT at a series of applied currents in a MEA. (b) FE_{CO} of AD-PTFE-CoPc/CNT at a wider range of series currents in MEA. (c, d) J_{CO} and EE of CO_2RR for CoPc/CNT, PTFE-CoPc/CNT, and AD-PTFE-CoPc/CNT.

Conclusion

In summary, we proposed a strategy to enhance the performance of molecular catalysts for CO_2RR by controlling the hydrophobicity with PTFE through crystallinity modulation. By leveraging interface adhesion during melt crystallization, CNTs modified with amorphism-dominated PTFE were obtained. Compared to spherulitic PTFE, the decrease in crystallinity resulted in increased polymer free volume and hydrophobic surface area, effectively strengthening the hydrophobicity of the CoPc microenvironment. The obtained catalyst achieved a maximum FE_{CO} of 96% in the MEA and maintained a consistent FE exceeding 85% at a total current of 0.8 A. Diffusion impedance testing and interface characterization jointly demonstrated the expansion of local CO_2 concentration, facilitating CO_2 adsorption coordination and thereby enhancing CO_2RR performance. This approach is believed to be flexibly applied to other molecular catalysts and different polymer systems. For phthalocyanine- and porphyrin-based molecular catalysts, where CO_2 adsorption and coordination were key steps for controlling reaction rate and selectivity, hydrophobic polymer modification effectively created a hydrophobic microenvironment that enhanced local CO_2 concentration. Additionally, by applying annealing treatments above the melting point of crystalline polymers, amorphism-dominated polymers with an expanded hydrophobic surface area were obtained. This study provided new insights into the regulation of PTFE hydrophobic modification and a general approach for enhancing the CO_2RR .



performance of molecular catalysts through interface engineering.

Author contributions

J.G. supervised the research. Z.Q., P.Z. and J.G. conceived the ideas and designed the experiments. Z.Q., H.Z., D.S., G.Z., H.G. and M.J. performed the experiments, device fabrication, electrochemical measurements, materials characterization and data analysis. Z.Q., P. Z., and J.G. wrote the manuscript. All authors discussed the experiments and commented on the manuscript.

Conflicts of interest

There are no conflicts to declare.

Data availability

The data supporting this article have been included as part of the Supplementary Information.

Acknowledgements

This work was supported by the National Key R&D Program of China (2021YFA1501503), the National Natural Science Foundation of China (22108197, 22121004, 22038009, and 22250008), the Haihe Laboratory of Sustainable Chemical Transformations (24HHWCSS00013), the Natural Science Foundation of Tianjin City (21JCZJC00060), the Program of Introducing Talents of Discipline to Universities (BPO618007) and the Xplorer Prize.

References

- D. D. Zhu, J. L. Liu and S. Z. Qiao, *Adv. Mater.*, 2016, **28**, 3423–3452.
- X. Du, P. Zhang, G. Zhang, H. Gao, L. Zhang, M. Zhang, T. Wang and J. Gong, *Natl. Sci. Rev.*, 2024, **11**, nwad149.
- G. Jiang, D. Han, Z. Han, J. Gao, X. Wang, Z. Weng and Q.-H. Yang, *Trans. Tianjin Univ.*, 2022, **28**, 265–291.
- D.-H. Nam, P. De Luna, A. Rosas-Hernández, A. Thevenon, F. Li, T. Agapie, J. C. Peters, O. Shekhal, M. Eddaoudi and E. H. Sargent, *Nat. Mater.*, 2020, **19**, 266–276.
- O. S. Bushuyev, P. De Luna, C. T. Dinh, L. Tao, G. Saur, J. van de Lagemaat, S. O. Kelley and E. H. Sargent, *Joule*, 2018, **2**, 825–832.
- P. De Luna, C. Hahn, D. Higgins, S. A. Jaffer, T. F. Jaramillo and E. H. Sargent, *Science*, 2019, **364**, eaav3506.
- H. Yao, M.-Y. Wang, C. Yue, B. Feng, W. Ji, C. Qian, S. Wang, S. Zhang and X. Ma, *Trans. Tianjin Univ.*, 2023, **29**, 254–274.
- Z. Gao, J. Li, Z. Zhang and W. Hu, *Chinese Chem. Lett.*, 2022, **33**, 2270–2280.
- S. Ren, D. Joulié, D. Salvatore, K. Torbensen, M. Wang, M. Robert and C. P. Berlinguette, *Science*, 2019, **365**, 367–369.
- F. Li, A. Thevenon, A. Rosas-Hernández, Z. Wang, Y. Li, C. M. Gabardo, A. Ozden, C. T. Dinh, J. Li, Y. Wang, J. P. Edwards, Y. Xu, C. McCallum, L. Tao, Z.-Q. Liang, M. Luo, X. Wang, H. Li, C. P. O'Brien, C.-S. Tan, D.-H. Nam, R. Quintero-Bermudez, T.-T. Zhuang, Y. C. Li, Z. Han, R. D. Britt, D. Sinton, T. Agapie, J. C. Peters and E. H. Sargent, *Nature*, 2020, **577**, 509–513.
- E. Boutin, M. Wang, J. C. Lin, M. Mesnage, D. Mendoza, B. Lassalle-Kaiser, C. Hahn, T. F. Jaramillo and M. Robert, *Angew. Chem. Int. Ed.*, 2019, **58**, 16172.
- Z. Jiang, Z. Zhang, H. Li, Y. Tang, Y. Yuan, J. Zao, H. Zheng and Y. Liang, *Adv. Energy Mater.*, 2023, **13**, 2203603.
- X. Kong, Y. Liu, P. Li, J. Ke, Z. Liu, F. Ahmad, W. Yan, Z. Li, Z. Geng and J. Zeng, *Appl. Catal. B-Environ.*, 2020, **268**, 118452.
- Y. Wu, Y. Liang and H. Wang, *Acc. Chem. Res.*, 2021, **54**, 3149–3159.
- R. Francke, B. Schille and M. Roemelt, *Chem. Rev.*, 2018, **118**, 4631–4701.
- L. Sun, V. Reddu, A. C. Fisher and X. Wang, *Energy Environ. Sci.*, 2020, **13**, 374–403.
- Y. Wu, G. Hu, C. L. Rooney, G. W. Brudvig and H. Wang, *ChemSusChem*, 2020, **13**, 6296–6299.
- X. Zhang, Y. Wang, M. Gu, M. Wang, Z. Zhang, W. Pan, Z. Jiang, H. Zheng, M. Lucero, H. Wang, G. E. Sterbinsky, Q. Ma, Y.-G. Wang, Z. Feng, J. Li, H. Dai and Y. Liang, *Nat. Energy*, 2020, **5**, 684–692.
- A. J. Sathrum and C. P. Kubiak, *J. Phys. Chem. Lett.*, 2011, **2**, 2372–2379.
- T. Burdyny and W. A. Smith, *Energy Environ. Sci.*, 2019, **12**, 1442–1453.
- M. Zhu, R. Ye, K. Jin, N. Lazouski and K. Manthiram, *ACS Energy Lett.*, 2018, **3**, 1381–1386.
- A. N. Marianov and Y. Jiang, *Acc. Mater. Res.*, 2022, **3**, 620–633.
- L. Sun, V. Reddu, S. Xi, C. Dai, Y. Sheng, T. Su, A. C. Fisher and X. Wang, *Adv. Energy Mater.*, 2022, **12**, 2202108.
- X. Zhang, Z. Wu, X. Zhang, L. Li, Y. Li, H. Xu, X. Li, X. Yu, Z. Zhang, Y. Liang and H. Wang, *Nat. Commun.*, 2017, **8**, 14675.
- J. Zhang, H. Chen, S. Liu, L.-D. Wang, X.-F. Zhang, J.-X. Wu, L.-H. Yu, X.-H. Zhang, S. Zhong, Z.-Y. Du, C.-T. He and X.-M. Chen, *J. Am. Chem. Soc.*, 2023, **145**, 20000–20008.
- F. Tang, Z. Wang, S. Wang, S. Xing, C. Li, S. Wang, Z. Jin and J.-B. Baek, *Chem. Eng. J.*, 2024, **487**, 150433.
- J. Ding, Z. Wei, F. Li, J. Zhang, Q. Zhang, J. Zhou, W. Wang, Y. Liu, Z. Zhang, X. Su, R. Yang, W. Liu, C. Su, H. B. Yang, Y. Huang, Y. Zhai and B. Liu, *Nat. Commun.*, 2023, **14**, 6550.
- S. Sato, K. Sekizawa, S. Shirai, N. Sakamoto and T. Morikawa, *Sci. Adv.*, 2023, **9**, eadh9986.
- Y. Jeong, Y. Kim, Y. J. Kim and J. Y. Park, *Adv. Sci.*, 2024, **11**, 2304735.
- K. H. Do, D. Praveen Kumar, A. Putta Rangappa, J. Wang, Y. Hong, E. Kim, D. Amaranatha Reddy and T. Kyu Kim, *Mater. Today Chem.*, 2021, **22**, 100589.
- T. Chan, C. J. Kong, A. J. King, F. Babbe, R. R. Prabhakar, C. P. Kubiak and J. W. Ager, *ACS Appl. Energy Mater.*, 2024, **7**, 3091–3098.
- P. Yue, Q. Fu, J. Li, L. Zhang, L. Xing, Z. Kang, Q. Liao and X. Zhu, *Chem. Eng. J.*, 2021, **405**, 126975.
- J. A. Rabinowitz, D. S. Ripatti, R. G. Mariano and M. W. Kanan, *ACS Energy Lett.*, 2022, **7**, 4098–4105.
- K. E. Rivera Cruz, Y. Liu, T. L. Soucy, P. M. Zimmerman and C. C. L. McCrory, *ACS Catal.*, 2021, **11**, 13203–13216.
- T. L. Soucy, W. S. Dean, J. Zhou, K. E. Rivera Cruz and C. C. L. McCrory, *Acc. Chem. Res.*, 2022, **55**, 252–261.
- C. M. Lieber and N. S. Lewis, *J. Am. Chem. Soc.*, 1984, **106**, 5033–5034.
- J. Lin, S. Yan, C. Zhang, Q. Hu and Z. Cheng, *ACS Appl. Mater. Interfaces*, 2022, **14**, 8623–8632.
- Z. Xing, X. Hu and X. Feng, *ACS Energy Lett.*, 2021, **6**, 1694–1702.
- L. Li, J. Chen, V. S. S. Mosali, Y. Liang, A. M. Bond, Q. Gu and J. Zhang, *Angew. Chem. Int. Ed.*, 2022, **61**, e202208534.
- X.-M. Hu, M. H. Rønne, S. U. Pedersen, T. Skrydstrup and K. Daasbjerg, *Angew. Chem. Int. Ed.*, 2017, **56**, 6468–6472.



- 41 B. Feng, Y. Li, S. Wu, H. Wang, Z. Tao and X. Fang, *Mater. Design*, 2016, **108**, 411–417.
- 42 M. Nofar, A. Tabatabaei, A. Ameli and C. B. Park, *Polymer*, 2013, **54**, 6471–6478.
- 43 M. Nofar, A. Tabatabaei and C. B. Park, *Polymer*, 2013, **54**, 2382–2391.
- 44 M. Nofar, W. Zhu and C. B. Park, *Polymer*, 2012, **53**, 3341–3353.
- 45 T. Y. Guo, Q. H. Zeng, C. H. Zhao, Q. L. Liu, A. M. Zhu and I. Broadwell, *J. Membrane Sci.*, 2011, **371**, 268–275.
- 46 Q. Fan, P. Hou, C. Choi, T. Wu, S. Hong, F. Li, Y. Soo, P. Kang, Y. Jung and Z. Sun, *Adv. Energy Mater.*, 2020, **10**, 1903068.
- 47 G. Dlubek, A. Sen Gupta, J. Pionteck, R. Häbeler, R. Krause-Rehberg, H. Kaspar and K. H. Lochhaas, *Polymer*, 2005, **46**, 6075–6089.
- 48 U. O. Nwabara, A. D. Hernandez, D. A. Henckel, X. Chen, E. R. Cofell, M. P. de-Heer, S. Verma, A. A. Gewirth and B. J. A. Kerns, *ACS Appl. Energy Mater.*, 2021, **4**, 5175–5186.
- 49 A. Huang, F. Liu, Z. Cui, H. Wang, X. Song, L. Geng, H. Wang and X. Peng, *Compos. Sci. Technol.*, 2021, **214**, 108980.
- 50 W. Kwon, J.-M. Kim and S.-W. Rhee, *Electrochim. Acta*, 2012, **68**, 110–113.
- 51 W. Zhang, J. Ma, P. Wang, Z. Wang, F. Shi and H. Liu, *J. Membrane Sci.*, 2016, **502**, 37–47.
- 52 S. S. Jeon, P. W. Kang, M. Klingenhof, H. Lee, F. Dionigi and P. Strasser, *ACS Catal.*, 2023, **13**, 1186–1196.
- 53 Z. Xing, L. Hu, D. S. Ripatti, X. Hu and X. Feng, *Nat. Commun.*, 2021, **12**, 136.
- 54 L. Xiong, X. Fu, Y. Zhou, P. Nian, Z. Wang and Q. Yue, *ACS Catal.*, 2023, 6652–6660.



The data that supports the findings of this study is available from the corresponding author upon reasonable request.

